Naval Research Laboratory

Washington, DC 20375-5320

High-Power, High-Intensity Laser Propagation and Interactions

P. Sprangle
B. Hafizi

Beam Physics Branch
Plasma Physics Division

March 10, 2014

REPORT DOCUMENTATION PAGE

1. REPORT DATE *(DD-MM-YYYY)* 10-03-2014	2. REPORT TYPE Interim	3. DATES COVERED *(From - To)* December 1984 – December 2014

4. TITLE AND SUBTITLE

High-Power, High-Intensity Laser Propagation and Interactions

5a. CONTRACT NUMBER

5b. GRANT NUMBER

5c. PROGRAM ELEMENT NUMBER

6. AUTHOR(S)

P. Sprangle* and B. Hafizi

5d. PROJECT NUMBER
67-4570-C3

5e. TASK NUMBER

5f. WORK UNIT NUMBER

7. PERFORMING ORGANIZATION NAME(S) AND ADDRESS(ES)

Naval Research Laboratory
4555 Overlook Avenue, SW
Washington, DC 20375-5320

8. PERFORMING ORGANIZATION REPORT NUMBER

NRL/MR/6703--14-9527

9. SPONSORING / MONITORING AGENCY NAME(S) AND ADDRESS(ES)

High Energy Laser-Joint Technology Office
801 University Blvd. SE, Suite 209
Albuquerque, NM 87106

10. SPONSOR / MONITOR'S ACRONYM(S)

HEL-JTO

11. SPONSOR / MONITOR'S REPORT NUMBER(S)

12. DISTRIBUTION / AVAILABILITY STATEMENT

Approved for public release; distribution is unlimited.

13. SUPPLEMENTARY NOTES

*Recipient of the James Clerk Maxwell Prize, Division of Plasma Physics, American Physical Society

14. ABSTRACT

This paper presents overviews of a number of processes and applications associated with high-power, high-intensity lasers and their interactions. These processes and applications include: free electron lasers, backward Raman amplification, atmospheric propagation of laser pulses, laser driven acceleration, atmospheric N_2 lasing, and remote detection of radioactivity. The interrelated physical mechanisms in the various processes are discussed.

15. SUBJECT TERMS

High-power lasers	Free electron lasers	Atmospheric lasings
High-intensity lasers	Radiation detection	Laser driven acceleration

16. SECURITY CLASSIFICATION OF:			17. LIMITATION OF ABSTRACT	18. NUMBER OF PAGES	19a. NAME OF RESPONSIBLE PERSON Phillip Sprangle
a. REPORT Unclassified Unlimited	**b. ABSTRACT** Unclassified Unlimited	**c. THIS PAGE** Unclassified Unlimited	Unclassified Unlimited	39	**19b. TELEPHONE NUMBER** *(include area code)* (202) 767-3493

Standard Form 298 (Rev. 8-98)
Prescribed by ANSI Std. Z39.18

High-Power, High-Intensity
Laser Propagation and Interactions

Phillip Sprangle and Bahman Hafizi

Plasma Physics Division
Naval Research Laboratory, Washington, DC 20375

Abstract

This paper presents overviews of a number of processes and applications associated with high-power, high-intensity lasers and their interactions. These processes and applications include: free electron lasers, backward Raman amplification, atmospheric propagation of laser pulses, laser driven acceleration, atmospheric lasing and remote detection of radioactivity. The interrelated physical mechanisms in the various processes are discussed.

_____

I. Introduction

High average power lasers, e.g., free electron lasers (FELs) and solid-state lasers (including fiber lasers) are prime candidates for efficient, directed energy applications. These include laser power beaming and laser weapons, requiring multi-kWs of CW power operating in the IR regime.

High-intensity lasers operate in a different regime, e.g., peak powers of $\sim 10^{12}$ - 10^{15} W, pulse lengths of $\sim 10^{-12} – 10^{-14}$ sec, intensities of $\sim 10^{14}$ - 10^{23} W/cm^2, and repetition rates ranging from $10^3 – 10^6$ Hz with average powers of > 10's W. These lasers are used in high-field physics research and have numerous potential applications. The physical processes associated with ultrashort pulse lasers (USPL) interactions include: photo/collisional ionization, Kerr and rotational Raman effects, self phase modulation, filamentation, group velocity dispersion, optical shocks, frequency chirping, etc. We discuss these interrelated physical processes and some of the applications of these lasers.

One of the important topics to be discussed in connection with both high-power and high-intensity lasers is propagation in a turbulent atmosphere. Laser propagation in atmospheric turbulence can results in beam centroid wander, spreading and intensity scintillation. A phase conjugation technique to mitigate the effects of atmospheric turbulence is described.

In Sec. II we discuss free electron lasers and related topics including optical guiding, efficiency enhancement, electron beam quality, coherent and incoherent x-ray FELs and backward Raman amplification. In Sec. III we discuss ultrashort pulse laser interactions and related topics, including atmospheric propagation of USPLs and laser driven electron acceleration in tapered plasma channels. In Sec.IV we discuss the role of atmospheric turbulence on the propagation of laser beams and also briefly discuss optical phase conjugation as a means to mitigate the effects of turbulence. In Sec. V we discuss various applications of high-power, high-intensity lasers including remote detection of radioactive material using electromagnetic signatures, atmospheric lasing of N_2 molecules. Concluding remarks are presented in Sec. VI.

II. Free Electron Lasers

Free electron lasers can generate high-power coherent radiation from the microwave to the x-ray regime [1-3]. The FEL mechanism is based on classical physics in which an electron beam induces radiation as it traverses a periodic magnetic field (wiggler) [4-13]. The FEL can operate in the low gain (interference, oscillator regime) [4] or a high gain (exponential, amplifier regime) [5]. One of the important characteristics of FELs is that the generated radiation beam can be guided by the electron beam, making possible extended interaction lengths. Also FEL efficiency can be enhanced by various methods such as spatially tapering the wiggler field. Free electron lasers are generally large, complex and expensive.

A schematic of an FEL is shown in Fig. 1. In this configuration, electron bunches from a radio frequency (RF) linac propagate through a wiggler and radiation is amplified by the electron-wiggler interaction. The spent electron beam is deflected either into a beam dump or re-circulated.
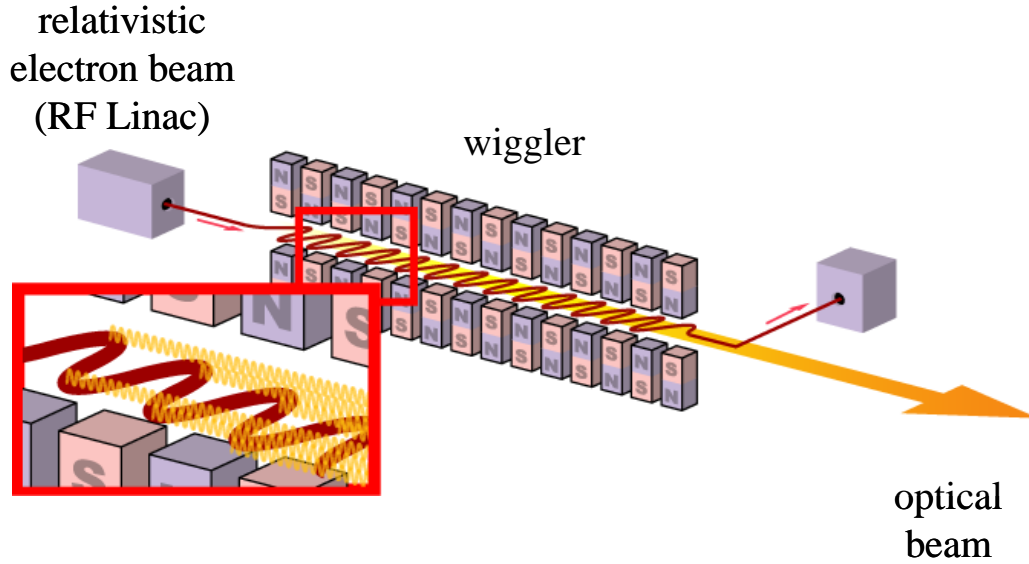

Figure 1. FEL amplifier configuration

Figure 2 is a schematic of an FEL employing a planar wiggler with period λ_W that is polarized along the x axis. An electron beam with relativistic factor γ propagates along

the z-axis and wiggles in the y-z plane. Radiation with wavelength λ that is polarized in the x direction, propagates in the z direction and is amplified provided $\lambda \approx \lambda_W / 2\gamma^2$.
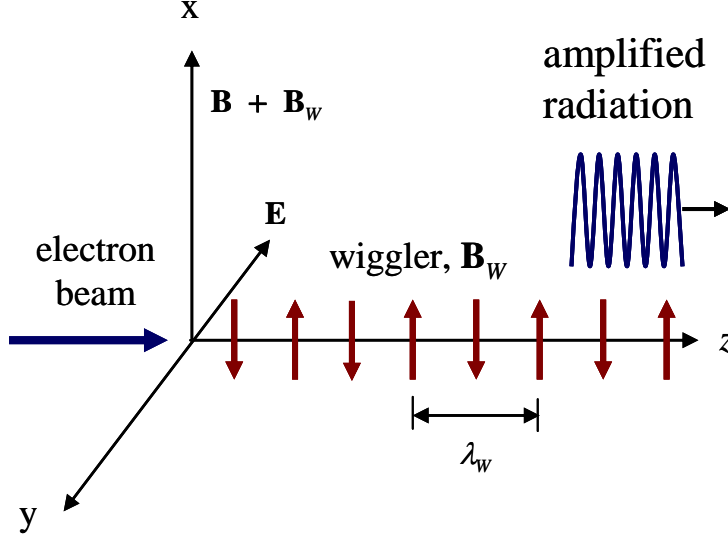

Figure 2. An electron beam interacts with a wiggler field and amplifies radiation propagating along the z-axis. The electron wiggle motion is in the y-z plane.

In the FEL a relativistic electron beam propagates through a combination of a wiggler field $\mathbf{B}_W = B_W \cos(k_W z)\hat{\mathbf{e}}_x$, and an optical radiation field

$\mathbf{E}_R = E\sin(k z - \omega t)\hat{\mathbf{e}}_y$, where $k_W = 2\pi/\lambda_W$, λ_W is the wiggler wavelength,

$k \approx \omega/c = 2\pi/\lambda$, λ is the radiation wavelength and $\hat{\mathbf{e}}_x$, $\hat{\mathbf{e}}_y$ denote transverse unit vectors. The essential feature of the FEL mechanism is that the beating of the fields causes the electrons to undergo axial bunching generating a beat wave. The axial force on the electrons is proportional to

$(q/c)\left(\mathbf{v}_W \times \mathbf{B}_R + \mathbf{v}_R \times \mathbf{B}_W \right)_z \sim \sin\left[(k + k_w)z - \omega t\right]\hat{\mathbf{e}}_z$, where $\mathbf{v}_W$ ($\mathbf{v}_R$) is the

transverse electron velocity due to the wiggler (radiation) field. This beat wave is referred to as the ponderomotive wave. The phase velocity of the ponderomotive wave $\omega/(k + k_W) < c$ is slightly less than the speed of light and comparable to the electron axial velocity v_z. The relativistic electrons can therefore transfer kinetic energy to the

radiation field, resulting in amplification. The electrons eventually become trapped in the ponderomotive wave and the radiation field saturates.

Greater insight into the FEL mechanism is provided by the one dimensional dispersion relation. The electron density wave, together with the electron wiggle motion, generate a transverse current having the proper phase, i.e., spatial – temporal, dependence to amplify the radiation field. The amplified radiation in turn enhances the electron density wave further amplifying the radiation. Considering spatial variations in the z direction only the FEL dispersion relation is [2]

$$\left(k^2 - \omega^2/c^2\right)\left((\omega - v_z(k + k_W))^2 - \omega_p^2/\gamma^3\right) = -4(\omega_p^2/\gamma)a_W^2 k_W^2, \qquad (1)$$

where $a_W = q B_W/mc k_W$ is the normalized wiggler amplitude and ω_b is the beam plasma frequency. The dispersion relation describes how the wiggler field couples the electromagnetic modes (first factor on the left hand side) to the electron beam modes (second factor on the left hand side).

a) Optical Guiding in FELs

In the FEL the wavefronts of the amplified radiation are such that the radiation tends to focus toward the electron beam [13]. Solving the dispersion relation, Eq. (1), the radiation wavenumber is found to be given by $k = \omega/c + \Delta k - i\Gamma$, where the wavenumber shift $\Delta k > 0$ when the growth rate is $\Gamma > 0$ (amplification). Since the refractive index associated with the radiation is $n = 1 + c\Delta k/\omega > 1$, the radiation undergoes focusing [13]. When focusing is balanced by diffraction the radiation beam is optically guided though the interaction region as shown in Fig.3. Optical guiding is important since the interaction length in the wiggler is generally long and diffraction would, in the absence of guiding, spread the radiation, terminating the FEL interaction.
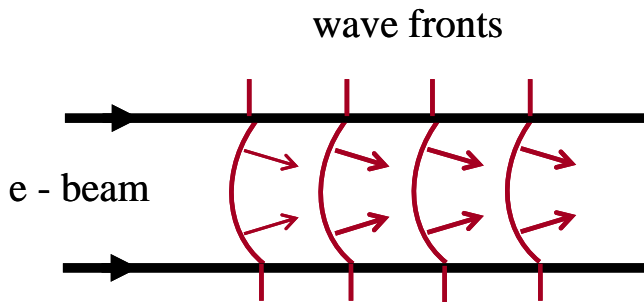

wave fronts

e - beam

Figure 3. Radiation beam is guided ($\Delta k > 0$) by electron beam in an FEL amplifier.

b) Efficiency Enhancement

Amplification of the radiation is at the expense of the electron beam kinetic energy. As the electrons slow down the FEL interaction coupling is reduced and efficiency decreases. However, by spatially tapering the wiggler field it is possible to reduce the phase velocity of the trapping (ponderomotive) wave to maintain synchronism with the electrons [11]. This is one of a number of methods to enhance the FEL efficiency. Figure 4 is a plot of the output power versus interaction length obtained from a simulation using the code GENESIS [14]. The electron and wiggler parameters on shown in the figure. The solid curve is for an untapered wiggler resulting in ~ 80 MW of output power while the dashed curve corresponds to a tapered case resulting in ~ 500 MW.
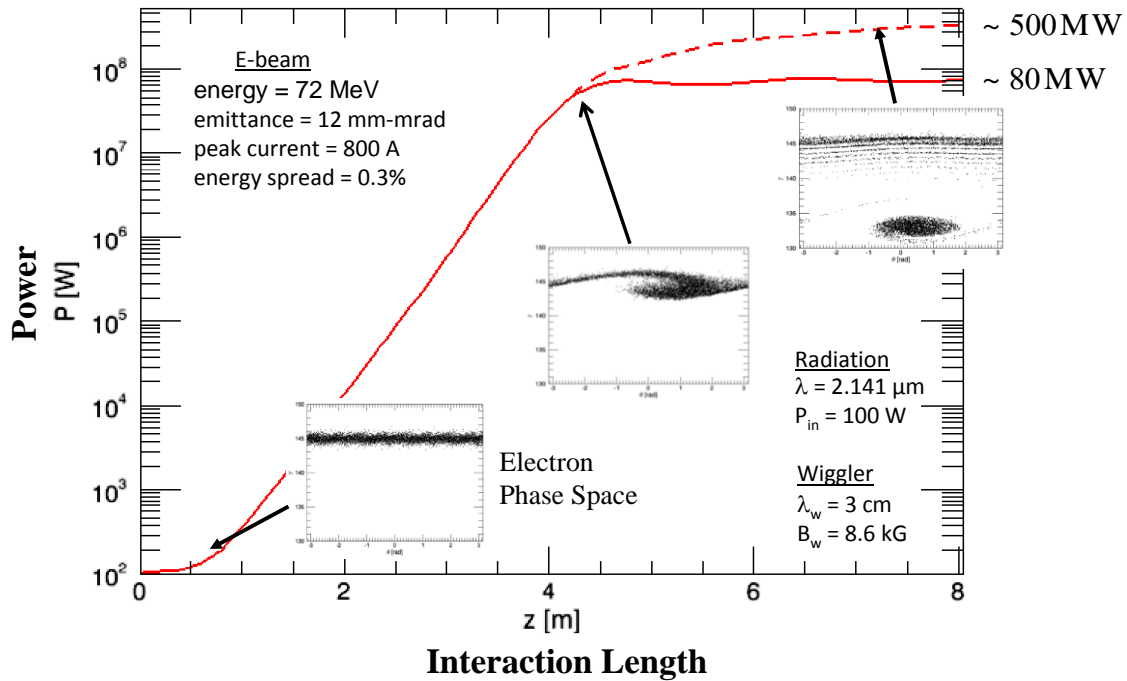

Figure 4. GENESIS simulation of FEL power versus interaction length without (solid curve) and with (dashed curve) tapering. The insets show the electron phase space (energy vs. ponderomotive phase) at various positions.

Theoretically and experimentally it has been demonstrated that the FEL mechanism can be reversed resulting in a laser driven electron accelerator [15].

6

c) Electron Beam Quality

In the FEL, the gain, growth rate and efficiency are sensitively dependent on the axial velocity spread $\Delta\beta_z$ of the electrons. The electron beam quality is measured in terms of emittance and energy spread, the origins of which include i) temperature of the cathode, ii) roughness of the emitting surface, iii) non-uniformity of the emission from the cathode surface, iv) nonlinearity of electric and magnetic fields, and v) self-fields. The electron beam quality requirement for the FEL is that $\Delta\beta_z$ be small compared to the efficiency $\lambda/2L_{eff}$ at the entrance to the wiggler where L_{eff} is the effective interaction length. This requirement can be expressed by the following inequality [2]

$$\Delta E_{total}/E < \lambda_w(1+a_w^2/2)/(4L_{eff}), \tag{2a}$$

where the total longitudinal energy spread is

$$\Delta E_{total}/E = \varepsilon_z/(\tau_b E) + \varepsilon_{n,\perp}^2/(2R_b^2) + \pi^2 a_w^2 R_b^2/(2\lambda_w^2). \tag{2b}$$

In Eq. (2b), the first term represents the fractional energy spread due to longitudinal emittance ε_z, the second term arises from transverse rms emittance $\varepsilon_{n,\perp}$, and the third term is due to transverse wiggler gradients. The right hand side of Eq. (2a) is the approximate FEL conversion efficiency, where the effective interaction length, L_{eff}, is the gain length in the case of the amplifier or the wiggler length in the case of the oscillator. If the inequality in Eq. (2a) is well satisfied the spread in the axial velocity of the electrons plays little role in the FEL interaction. As an example, for a MW-class FEL operating in the IR regime, the typical parameters are $\varepsilon_{n,\perp} \approx 15\,\text{mm mrad}$, $\varepsilon_z \approx 100\,\text{keV psec}$, $R_b \approx 0.3\,\text{mm}$, $\tau_b \approx 1\,\text{psec (rms)}$, $E = 80\,\text{MeV}$, $a_w^2 = 2$, and $\lambda_w = 3\,\text{cm}$ [16]. For these parameters $\varepsilon_z/(\tau_b E) \leq 0.13\%$, $\varepsilon_{n,\perp}^2/(2R_b^2) \approx 0.13\%$, $\pi^2 a_w^2 R_b^2/(2\lambda_w^2) \approx 0.1\%$ and $\Delta E_{total}/E \approx 0.36\%$. For an amplifier having a gain length of $30\,\text{cm}$ the right hand side of Eq. (2a) is $\approx 5\%$ and the inequality is well satisfied. For an oscillator the right hand side of Eq. (2a) is $\sim 1/2N_w$, where N_w is the number of wiggler periods. For $N_w = 100$ the inequality is also satisfied.

d) Coherent and Incoherent X-Ray FELs

The FEL can generate coherent, polarized, short pulses of x-rays for numerous applications in research. A number of large-scale electron accelerator facilities throughout the world are being used (or will be commissioned soon) for coherent x-ray generation using a conventional FEL configuration [17-20]. Generation of x-rays at these facilities typically requires electron beam energies in the multi-GeV range with peak currents in the multi-kA range, and wiggler lengths of many tens of meters. An x-ray FEL amplifier can be operated in the self-amplified regime, eliminating the need for a coherent input x-ray source [21-23].

The wiggler field in the FEL can be replaced with an intense laser beam propagating anti-parallel to the electron beam [24]. In a laser pumped x-ray FEL electron beam energies in the multi-MeV range would be sufficient, leading to a more compact device. However, a number of major challenges would have to be overcome before a laser pumped coherent x-ray FEL would be feasible, e.g., ultra-high electron beam brightness. A compact source of incoherent x-rays can be configured in which microwaves or laser radiation is Compton backscattered off a relativistic electron beam [25-27].

e) Backward Raman Amplification

In the backward Raman amplification (BRA) scheme, two counter propagating laser beams are resonantly coupled by a plasma wave [28-30]. The laser beams have a frequency difference which is approximately equal to the plasma frequency. The higher frequency (ω_o), long pulse pump laser supplies energy to the lower frequency ($\omega_1 \approx \omega_o - \omega_p$), short pulse seed laser which undergoes amplification and pulse compression. The phase velocity of the plasma wave is in the same direction as the pump laser.

The BRA in the linear regime is fundamentally the same as the FEL mechanism in the frame of the electron beam. In the electron beam frame the wiggler field is essentially a counter propagating electromagnetic wave. Thus, replacing the wiggler field in Eq.(1) with a counter propagating laser beam results in the BRA dispersion relation. By setting $v_z = 0$ in the FEL dispersion relation, Eq.(1), with appropriate redefinition of symbols the BRA dispersion relation is obtained

$(k^2 - \omega^2/c^2)((\omega - \omega_o)^2 - \omega_p^2) = -2\omega_p^2 \, a_o^2 \, k_o^2$ and sketched in Fig. 5. In the BRA process the seed laser grows and is temporally compressed at the expense of the pump laser. This process can generate high intensity ultra-short laser pulses. Experiments have demonstrated amplification of seed intensities by a factor of 10^4 with an efficiency of > 6% [31,32].
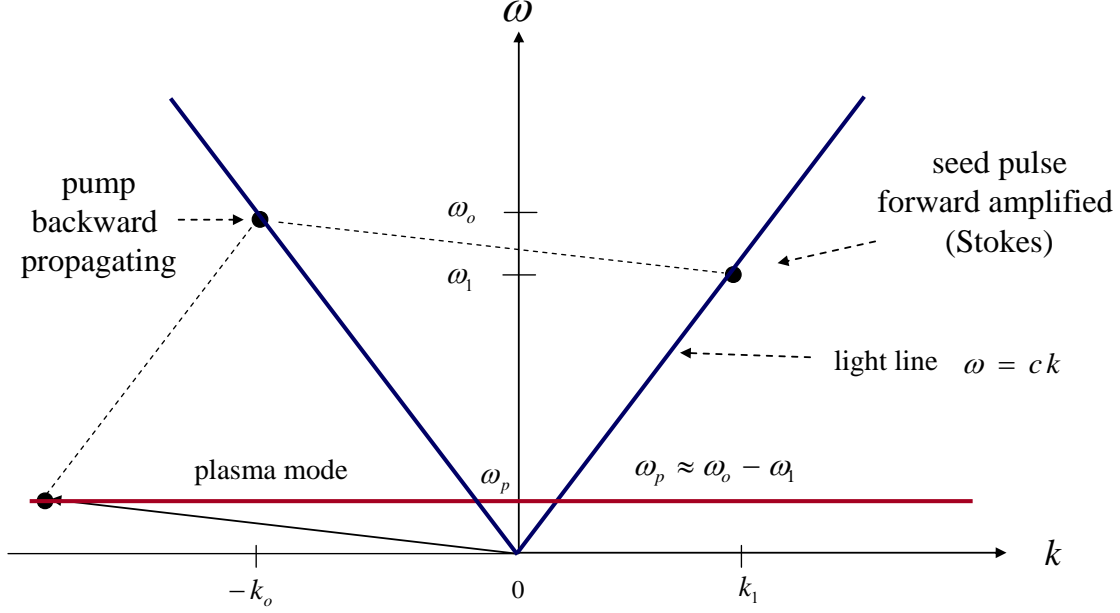

Figure 5. Dispersion diagram describing the backward Raman amplification process. This dispersion diagram also describes the FEL process in the beam frame.

III. Ultra Short Pulse Laser Interactions

A great deal of progress has been made in the development of ultra-short pulse lasers (USPL) [33]. Table I lists some of the important parameters associated with these lasers.

Peak power	10^{12} - 10^{15} W
Intensity	10^{13} - 10^{23} W/cm^2
Pulse duration	10^{-12} - 10^{-14} sec
Average power	< 100 W

Table I. Range of parameters for ultrashort pulse lasers

9

Ultrashort pulse lasers have numerous applications, including i) laser driven electron and ion acceleration (plasma, Cherenkov, vacuum); ii) laser synchrotron (Compton backscattering) source of x-rays; iii) remote sensing and radioactivity detection and iv) remote atmospheric lasing.

a) Atmospheric Propagation of Ultrashort Pulse Lasers

Atmospheric propagation of USPLs with ~ TW power levels and pulse durations of ~ 100 fsec is strongly affected by various, interrelated linear and nonlinear processes [33-41]. These include diffraction, Kerr focusing, group velocity dispersion, spectral broadening, self-phase modulation, photo-ionization, plasma defocusing, and energy depletion due to both ionization and ohmic heating. A laser pulse propagating in air can be longitudinally and transversely focused at remote distances (> km) to reach intensities which will ionize the air. Longitudinal pulse compression is achieved by introducing a negative frequency chirp on the pulse while nonlinear transverse focusing is caused by the Kerr effect (see Fig. 6). As a result of the focusing, the laser intensity is greatly enhanced ($> 10^{13}$ W/cm^2), resulting in tunneling ionization of air and a localized plasma filament ~ 1 m in length, ~ 100 μm in radius, having an electron density of $\sim 10^{16}$cm^{-3} and a temperature of ~1eV [40]. While undergoing filamentation (plasma formation) the intensity of the USPL is depleted due to ionization losses or diffraction and has a typical propagation range of many tens of meters. The length of the filament is determined by air chemistry processes such as electron recombination and attachment.
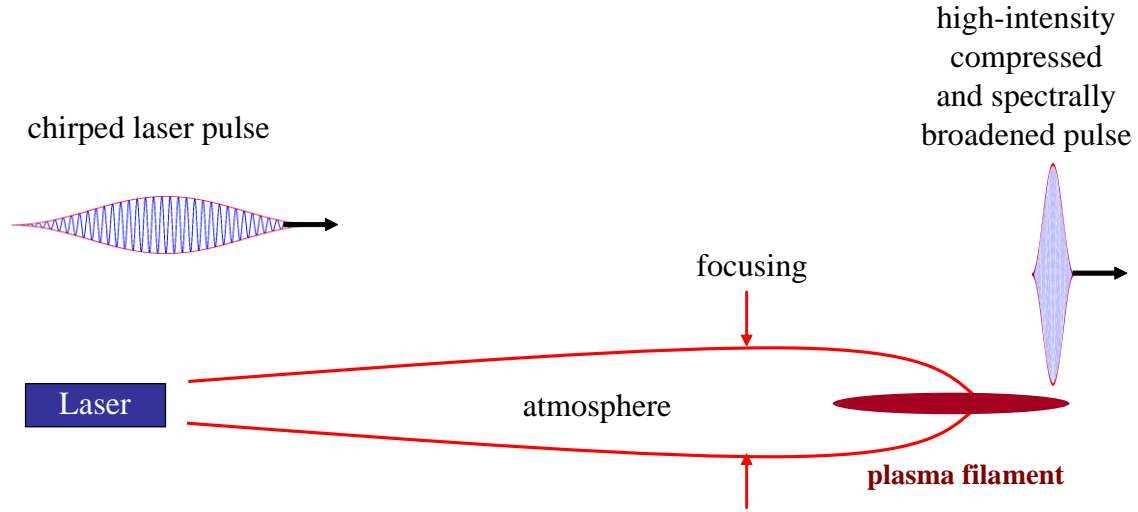
Figure 6, Atmospheric propagation, filamentation and spectral broadening

The propagation of USPLs in the atmosphere may have important applications in the areas of active and passive remote sensing, electronic countermeasures and induced electric discharges, e.g., artificial lightning. For example, localized ultraviolet radiation generated at a remote distance by laser ionization can provide a source for active fluorescence spectroscopy of biological and chemical agents in the atmosphere. Pulses of intense, directed white light may also find applications in the areas of hyperspectral imaging and differential absorption spectroscopy. The nonlinearities associated with the air and plasma filament can result in super-continuum spectral broadening of the USPL and ultraviolet radiation.

Experiments using ultrashort, high intensity laser pulses have demonstrated atmospheric propagation, air breakdown, filamentation, and white light generation [42-45]. Intense, directed white light pulses have been generated and backscattered from atmospheric aerosols up to altitudes of ~15 km [37]. The generation of THz radiation by femtosecond pulses has also been observed and analyzed [46,47].

Filamentation in Air

Hot spots on the intensity profile of a laser beam can grow as a result of a filamentation instability. Filamentation, i.e., transverse break-up of a laser beam is due to the interplay between diffraction and nonlinear self-focusing (Kerr effect). Consider a

laser beam propagating in a neutral gas for which the nonlinear focusing power is
$P_K = \lambda^2 / (2\pi n_K)$ where n_K is the Kerr effect contribution to the refractive index and the
transverse laser intensity profile is slightly perturbed by a small, localized hot spot. The
spatial growth rate of this filamentation instability [40] is

$$\Gamma = \frac{\lambda}{\pi x_\perp} \left(\frac{3\pi I}{P_K} - \frac{1}{x_\perp^2} \right)^{1/2} , \tag{3}$$

where I is the laser intensity and $x_\perp$ is the characteristic transverse dimension of the
filament, i.e., spot size. As a function of the dimension of the filament, the growth rate
vanishes for $x_\perp \leq x_{min} \equiv [P_K / (3\pi I)]^{1/2}$, reaches a maximum equal to
$\Gamma_{max} = 3\lambda I / (2P_K)$ at $x_\perp = \sqrt{2} x_{min}$, and decreases inversely with $x_\perp$ as $x_\perp$ increases.
At maximum growth rate the power within the filament is roughly equal to P_K. It is
therefore expected that a laser beam with a power P will break-up into N filaments where
$N \leq P / P_K$. As an example, the nonlinear focusing power associated with air for a
$1\,\mu m$ wavelength, ~ 1 nsec duration laser is in the range of ~ 3 GW
($n_K \sim 5.6 \times 10^{-19}\,cm^2/W$) [48,49]. For example, a 3 TW laser pulse can eventually break-
up into ~ 10^3 filaments, see Fig.7 [42].
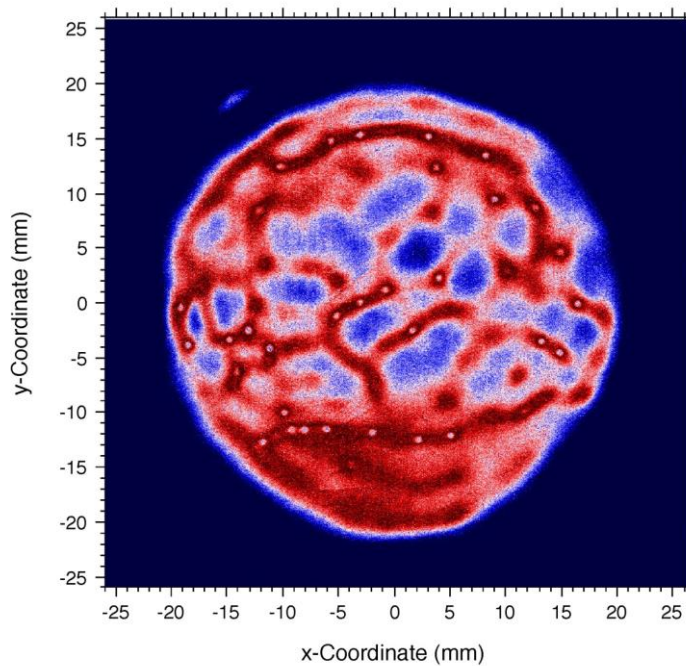

Figure 7: Filamentation of a
400 fs, $\lambda = 1.05\,\mu m$ USPL
after 13 m of propagation in
air.

The free electron density in air can change because of ionization, recombination and attachment processes. The rate equation for electron density N_e is [50-53]

$$\frac{\partial N_e}{\partial t} = W N_{air} - \eta N_e - \beta_e N_e^2,$$ (4)

where W is the photoionization rate, $N_{air} = 2.7 \times 10^{19}\, cm^{-3}$ is the air density, η is the electron attachment rate and β_e is the electron-ion dissociation recombination rate. Typical values for the attachment and recombination coefficients are $\eta \sim 10^8\, sec^{-1}$ and $\beta_e \sim 3 \times 10^{-8}\, cm^3 sec^{-1}$. For short laser pulses, free electrons are generated by multi-photon and tunneling processes; avalanche ionization is not significant for USPLs

The length of the plasma filament is determined by the electron attachment and recombination coefficients and from Eq.(4) and is given by $\ell_{filament} \sim c/(\eta + \beta_e N_e) < 2\,m$. The USPL loses energy through ionization and has a propagation length of $L_{depletion} \approx P \tau_L /(U_{ion} N_e \pi R_o^2 / 2) \sim 100\,m$, where P is the laser power, τ_L is the pulse length and U_{ion} is the ionization potential (see Fig 8). The balancing of Kerr focusing and plasma defocusing leads to intensity clamping of the USPL which is typically $I_{clamp} \sim 10^{13} - 10^{14}\, W/cm^2$.
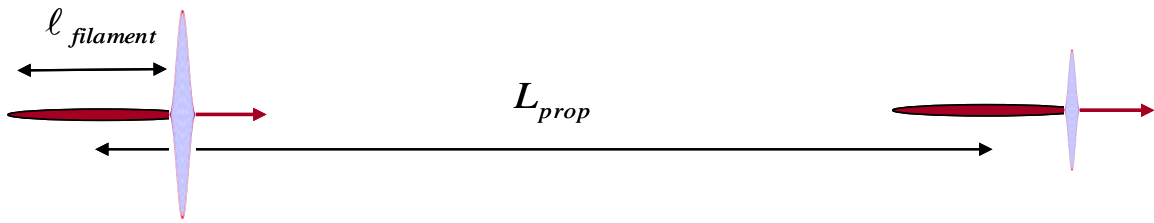

Figure 8. USPL filamentation, indicating filament length and propagation limits.

b) Laser Driven Acceleration

The extremely large field associated with USPLs propagating in plasmas can generate plasma waves which trap and accelerate electrons [54-68]. In the standard laser wakefield accelerator (LWFA), a short laser pulse, on the order of a plasma wavelength

long, excites a trailing plasma wave that can trap and accelerate electrons to high energy (see Fig.9). Numerous analyses and experiments have been performed to characterize and advance the LWFA concept. However, there are a number of issues that must be resolved before a practical high-energy accelerator can be developed. These include Raman, modulation and hose instabilities that can disrupt the acceleration process [68]. In addition, extended propagation of the laser pulse is necessary to achieve high electron energy.

In the absence of optical guiding the acceleration distance is limited to a few Rayleigh ranges $Z_R = \pi R_o^2 / \lambda \sim 1\,\text{cm}$ which is far below what is necessary to reach GeV electron energies [54]. The diffraction limitation can be mitigated by employing a plasma channel in which the plasma density increases as r^2. The physics of laser beams propagating in plasma channels has been studied [56,64,68,69] and there is ample experimental confirmation of extended guided propagation in plasmas and plasma channels [70-76]. In addition, dephasing of electrons in the wakefield can limit the interaction length to $(\lambda_p / \lambda)^2 \lambda_p \sim 30\,\text{cm}$ and, therefore, limit the energy gain. By increasing the plasma density as a function of distance, the phase velocity of the accelerating field behind the laser pulse can be made equal to the speed of light. Thus, electron dephasing in the accelerating wakefield can be postponed and energy gain increased by spatially tapering the plasma channel. Staging LWFAs can be used to overcome the laser energy loss limitation. Injection, trapping and acceleration in the wakefield continues to be of interest [77].
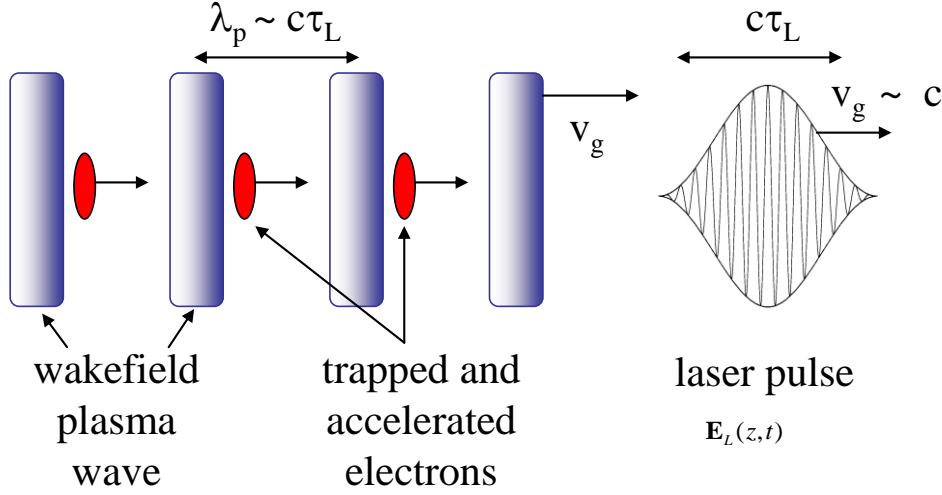
Figure 9. Schematic of laser wakefield accelerator mechanism

A simplified, one-dimensional model of the laser wakefield accelerator driven by the ponderomotive force induced by the USPL is shown in Fig.9 [54]. The ponderomotive force $F_{pond} = q(\mathbf{v} \times \mathbf{B}/c)_z = -(q^2/2m\omega^2)\partial(\mathbf{E}_L \cdot \mathbf{E}_L)/\partial z$ associated with the laser pulse generates large amplitude plasma waves (> 100 GV/m) that can accelerate self-trapped or injected electrons to high energies.

The plasma density wave (wakefield) is driven by the ponderomotive force and satisfies a driven harmonic oscillator equation

$$\frac{\partial^2 \delta N_p}{\partial t^2} + \omega_p^2 \delta N_p = N_{po} c^2 \frac{\partial^2}{\partial z^2}\left(\frac{q\hat{E}}{2mc\omega}\right)^2, \tag{5}$$

where ω_p is the plasma frequency N_{po} is the unperturbed plasma density, δN_p is the perturbed density (wakefield) and $E_L(z,t) = \hat{E}(z,t)\sin(kz - \omega t)$ the laser field. The accelerating wakefield (space charge field) is given by $\partial E_{accel}/\partial z = 4\pi q \delta N_p$. The accelerating gradient $|E_{accel}|$ is proportional to $\sim \sqrt{N_p}\, I$, where $I = c|\hat{E}|^2/8\pi$ is the intensity, and can be $\sim 10^3$ times greater than accelerating gradients in RF accelerators.

i) Optical Guiding in LWFA

The laser spot size $R(z)$ as a function of axial position in a plasma with refractive index n is given by [64]

$$\frac{\partial^2 R}{\partial z^2} = \frac{\lambda^2}{\pi^2 R^3} + \frac{2}{R}\left\langle r\frac{\partial n}{\partial r}\right\rangle, \tag{6}$$

where $\langle ...\rangle$ is an average performed using the laser intensity as the weighting function. The full refractive index associated with the laser plasma interaction having a parabolic density variation in the radial direction is

$$n(r) = 1 - \frac{\omega_{po}^2}{2\omega^2}\left(1 - \frac{\beta_{os}^2(r)}{4} + \frac{\delta N_p}{N_{po}} + \frac{\Delta n}{N_{po}}\frac{r^2}{R_o^2}\right) \tag{7}$$

The expression for the refractive index is obtained by noting that $\omega_p(r) = (4\pi q^2 N_p(r)/\gamma(r)m)^{1/2}$ is the plasma frequency, where $N_p(r) = N_{po} + \Delta n\, r^2/R_o^2$ is the plasma density in the channel, $\gamma(r)$ is the relativistic mass factor, $\beta_{os}(r) = q\hat{E}(r)/(mc\omega)$, $\omega_{po} = \omega_{po}(r=0)$ and $N_{po} = N_p(r=0)$. For short laser pulses $c\tau_L \leq \lambda_p$ the relativistic term $\beta_{os}^2/4$ just cancels the wakefield term $\delta N_p/N_{po}$. In the short pulse limit the laser spot size dynamics in a plasma channel is given by

$$\frac{\partial^2 R}{\partial z^2} = \frac{R_o^4}{Z_R^2}\left(1 - \frac{\Delta n}{n_C}\frac{R^4}{R_o^4}\right)\frac{1}{R^3}, \tag{8}$$

where $n_C = 1/(\pi r_e R_o^2)$ is the depth of the plasma channel and r_e is the classical electron radius (see Fig.10). Note that in the absence of a plasma wave and plasma density channel, i.e., uniform plasma density, optical guiding is possible through a relativistic effect. Here the laser power must equal the relativistic focusing power, which is

$$P_{rel}[GW] = 17.4\,(\omega/\omega_p)^2.$$

plasma density

refractive index

laser profile (Gaussian)

$n_c = 1/(\pi\, r_e\, R_o{}^2) \sim 10^{17}\ cm^{-3}$
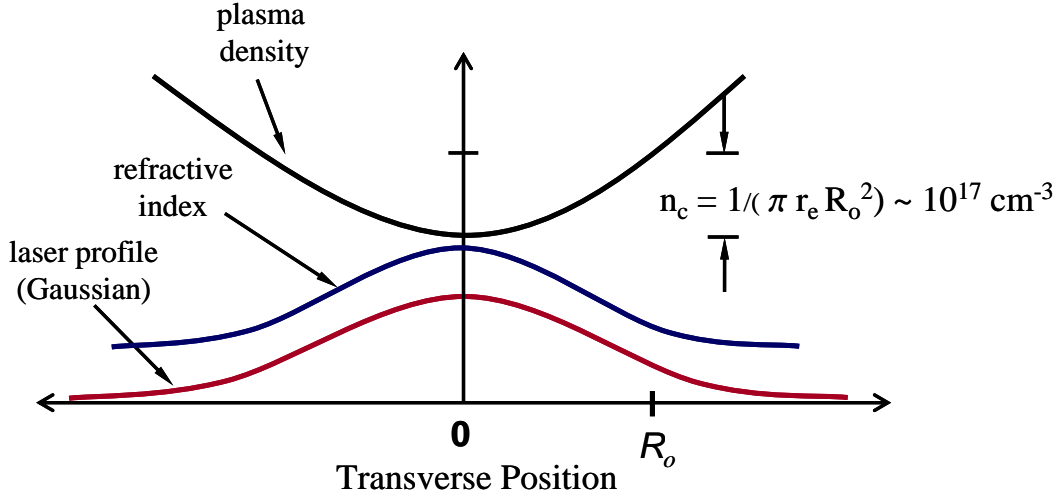
0

R_o

Transverse Position

Figure 10. Guided propagation of Gaussian laser beam in a parabolic-profile plasma density. In a plasma channel the guiding condition is independent of wavelength.

Extended optical guiding is important for achieving significant energy gain in the LWFA. Laser wakefield experiments at LBNL employing optical guiding of a 40 TW laser pulse in a gas jet configuration resulted in observation ~ GeV electrons [78].

ii) Raman and Modulational Instabilities

The dynamics of a laser pulse propagating in a uniform plasma channel is affected by Raman and modulational instabilities. In the broad beam limit $(R_o >> c\tau_L)$, however, the nonlinear terms in the wave equation that lead to Raman and modulation instabilities tend to cancel [79]. This can result in pulse propagation over extended distances, limited only by dispersion with minimal pulse distortion due to instabilities.

iii) LWFA in a Tapered Plasma Channel

By employing a tapered plasma channel electron-wakefield dephasing, i.e., slippage, can be postponed [80,81]. The phase of the wakefield behind the laser pulse is $\psi(z,\tau) = \omega_p(z)(\tau - \tau_L/2)$ and the phase velocity is given by

$$v_{ph}(z,\tau) = \frac{v_g(z)}{\left[1 - \left(\partial\omega_p(z)/\partial z\right)\left(v_g(z)/\omega_p(z)\right)\left(\tau - \tau_L/2\right)\right]},\qquad(9)$$

where $\tau = t - \int_0^z dz'/v_g(z')$ is the time measured in the frame of the pulse with group velocity $v_g(z)$ and τ_L is the laser pulse length. The phase velocity of the wakefield

varies with distance behind the pulse. The phase velocity increases (decreases) with distance from behind the pulse for an increasing (decreasing) plasma density. The location behind the pulse, τ_c, for which the phase velocity equals the speed of light in vacuum is given by

$$c\,\tau_c(z) = \frac{\omega_p^2/(2\,\omega_o^2) + 2\,c^2/(\omega_o^2\,R_o^2)}{\partial \ln \omega_p / \partial z} + \frac{c\,\tau_L}{2}. \qquad (10)$$

The solid curve in Fig. 11 shows the energy of a test electron along a tapered plasma channel (increasing plasma density) that is trapped and accelerated to ~ 4 GeV. The dashed curve shows an energy gain of ~ 1GeV in an untapered channel.
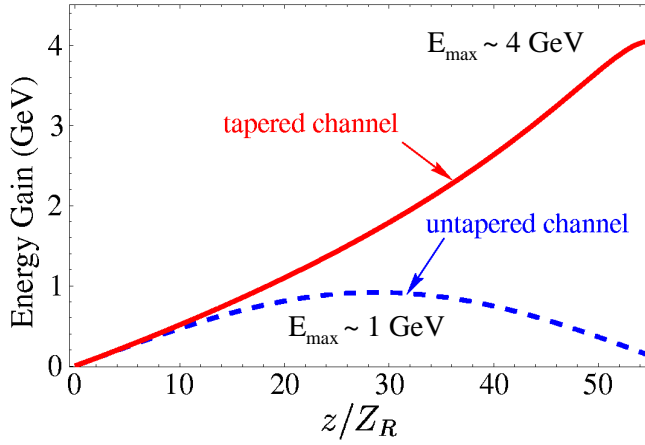

Figure 11. Energy gain as a function of propagation distance normalized to the Rayleigh range Z_R. Dashed curve is for an untapered channel (maximum energy ~ 1 GeV) while the solid curve is for a tapered channel (maximum energy ~ 4 GeV).

Spatially periodic plasma channels, with periods as small as $\sim 50\,\mu m$, have been demonstrated [82]. The modulated plasma channel can support lower phase velocity wakefields which can more readily trap low energy electrons and accelerate them into higher phase velocity wakefields.

IV. Laser Propagation in Atmospheric Turbulence

Atmospheric turbulence, absorption, scatterings, scintillation and thermal blooming can have an important effect on laser propagation [83]. The following discussion deals primarily with laser propagation through atmospheric turbulence. The refractive index of turbulent air is $n = 1 + \delta n(x, y, z, t)$, where $\langle \delta n \rangle = 0$ and $\langle \delta n^2 \rangle \neq 0$.

The strength of the turbulence is characterized by the structure parameter C_n^2 which typically is in the range of $10^{-15} - 10^{-13}\,\mathrm{m}^{-2/3}$ at ground level [83-85].

Turbulence leads to an increase in spreading of the laser beam spot size, R_s. In addition, turbulence leads to wandering of the laser beam centroid, R_w Figure 12 shows the laser beam spot (small circles) at several instants in time. Over a time scale that is long compared with that associated with wander one obtains the broadened spot shown by the large dotted circle in Fig.12.

The time averaged laser spot size $R(L)$ at range L is given by

$$R^2(L) = (\lambda L / \pi R_o)^2 (M^4 + 2.9(R_o / r_o)^2) + \theta_{jitter}^2 L^2 + R_o^2 (1 - L / L_f)^2, \quad (11)$$

where $R \approx (R_w^2 + R_s^2)^{1/2}$, R_o is the initial spot size, λ is the laser wavelength, M^2 is the intrinsic laser beam quality, L_f is the focal length, r_o is the transverse coherence length associated with turbulence and θ_{jitter} is the mechanical jitter angle of the beam. For a constant value of C_n^2 the transverse coherence length is $r_o = 0.184(\lambda^2 / C_n^2 L)^{3/5}$. However, as far as laser beam propagation is concerned the effective strength of turbulence is not determined by C_n^2 alone, but also depends on the range of propagation and the wavelength. The relevant combination is the Rytov variance, defined by $\sigma_R^2 = 10.5 C_n^2 \lambda^{-7/6} L^{11/6}$. For weak turbulence ($\sigma_R^2 < 0.3$), beam wander and spreading are distinct and tip-tilt compensation can be used to correct for beam centroid wander. On the other hand, for strong turbulence ($\sigma_R^2 > 0.3$) the beam breaks up into multiple beams and beam wander and spreading are not distinct, hence, tip-tilt compensation is less effective. The Rytov variance is a measure of the intensity scintillation level on axis at the target, i.e., $\sigma_R^2 = \left\langle \left(I - \langle I \rangle \right)^2 \right\rangle / \langle I \rangle^2$ for weak turbulence.
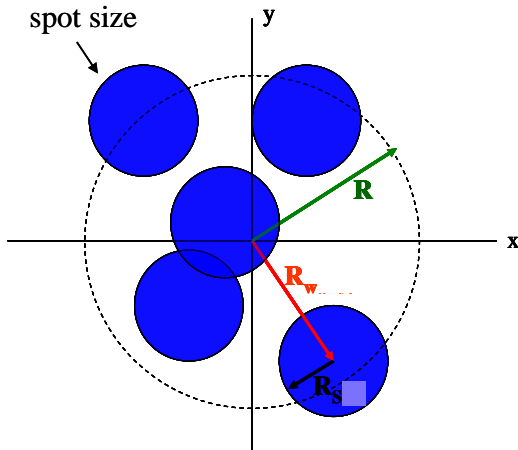

Figure 12. Schematic showing the effects of turbulence on beam propagation, R_w is the centroid displacement (wander), and R_S is the increase in spot size (spreading), where $R \approx (R_w^2 + R_s^2)^{1/2}$.

19

Figure 13 shows the laser intensity contours for three levels of atmospheric turbulence. In limit of extremely weak turbulence ($C_n^2 = 0$, $\sigma_R^2 = 0$, Fig.13(a)) the laser intensity is well-defined with a relatively small spot size [86]. In moderate turbulence ($C_n^2 = 10^{-14}\, m^{-2/3}$, $\sigma_R^2 \approx 0.1$, Fig.13(b)) the laser profile is distorted and the spot size is larger. In strong turbulence ($C_n^2 = 10^{-13}\, m^{-2/3}$, $\sigma_R^2 \approx 1$, Fig.13(c)) the laser profile is highly distorted. For sufficiently strong turbulence a single discernable high-intensity region in the cross-section may not be obtained.
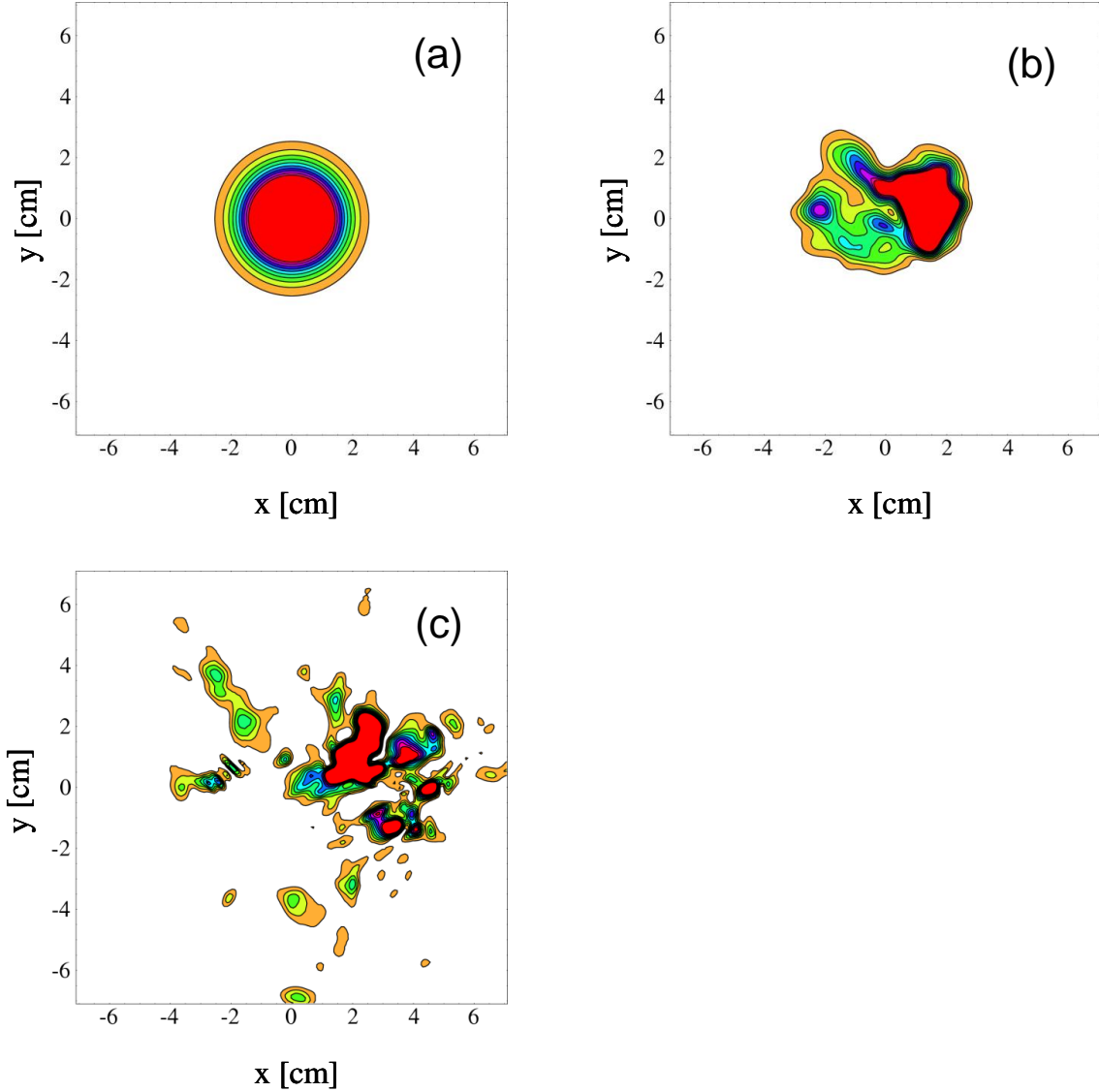

Figure 13. Comparison of the intensity contours in the x-y plane at a range of 0.5 km for three levels of turbulence using the propagation code HELCAP [86].

Effective beam control of high energy lasers (HELs) is a key component of a laser directed energy system. Strong turbulence can have a significant deleterious effect on the propagation of the HEL beam. By appropriately modifying the wavefront of the transmitted beam the laser power can be more effectively focused on target [87,88]. A beacon beam can be used to record the atmospheric phase aberrations used to modify the amplitude and phase of the transmitted high power beam; see Fig.14 for a simplified view of the process. The information needed for modifying the amplitude and phase is obtained by phase conjugating the beacon beam, i.e., $\exp(i\mathbf{k}\cdot\mathbf{r}) \Rightarrow \exp(-i\mathbf{k}\cdot\mathbf{r})$. Phase conjugation can be achieved by using deformable mirrors or by a nonlinear optical mixing mechanism, e.g., 4-wave Brillouin mixing [89,90].

transmitted beam
is phase conjugated

turbulent air
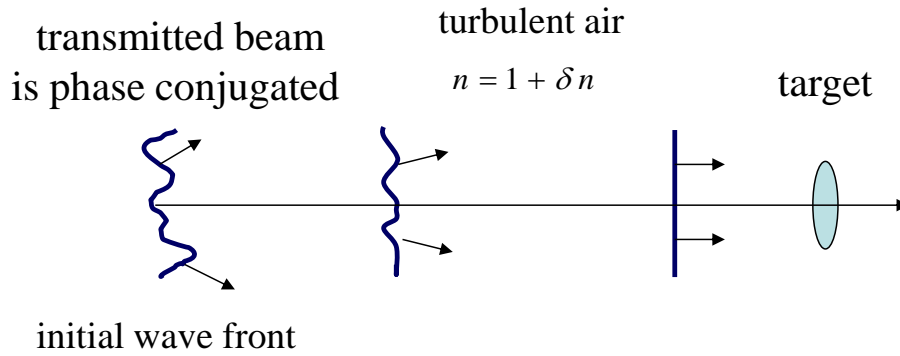$n = 1 + \delta n$

target

initial wave front

Figure 14. Using phase and amplitude information provided by a beacon beam the distortion of the transmitted high power laser beam is gradually undone as it propagates to the target.

V. Applications of High-Power, High-Intensity Lasers

Advances in FELs and solid-state lasers (including fiber lasers) have made them prime candidates for high-average power applications. These include power beaming and directed energy applications. In this section we discuss remote detection of radioactive material and remote atmospheric lasing for chemical/biological detection, employing high-intensity lasers.

a) Remote Detection of Radioactive Material

A recently proposed radioactivity detection concept is based on a high power THz pulse inducing avalanche breakdown and spark formation in the vicinity of the radioactive material [91,92]. In this detection concept the time delay for spark formation and the breakdown rate, which are functions of the initial ion and electron densities, can provide a direct signature for the presence of radioactivity.

We discuss a new concept which is based on the detection of electromagnetic signatures in the vicinity of radioactive material and can enable stand-off detection [93]. Radioactive materials emit gamma rays which ionize the surrounding air. The ionized electrons rapidly attach to oxygen molecules forming O_2^- ions. The density of O_2^- around radioactive material can be several orders of magnitude greater than background levels. The elevated population of O_2^- extends several meters around the radioactive material. Electrons are easily photo-detached from O_2^- ions by laser radiation. The photo-detached electrons, in the presence of laser radiation, initiate avalanche ionization which results in a rapid increase in electron density. The rise in electron density induces a frequency modulation on a probe beam which becomes a direct spectral signature for the presence of radioactive material [93].

High-power, short-pulse lasers propagating in the atmosphere can come to a focus in the vicinity of the radioactive material by making use of longitudinal compression and transverse focusing, see Sec. IIIa and [40]. The negative ions produced by the radioactive material have an electron affinity resulting in a low ionization potential of 0.46 eV and can be photo-detached by laser radiation ($\sim 0.8-1\mu m$). The detection concept is based on a probe radiation beam undergoing a frequency modulation while propagating in a temporally increasing electron density. The frequency modulation on the probe beam becomes a spectral signature for the presence of radioactive material. A schematic of the detection concept is shown in Fig.15.
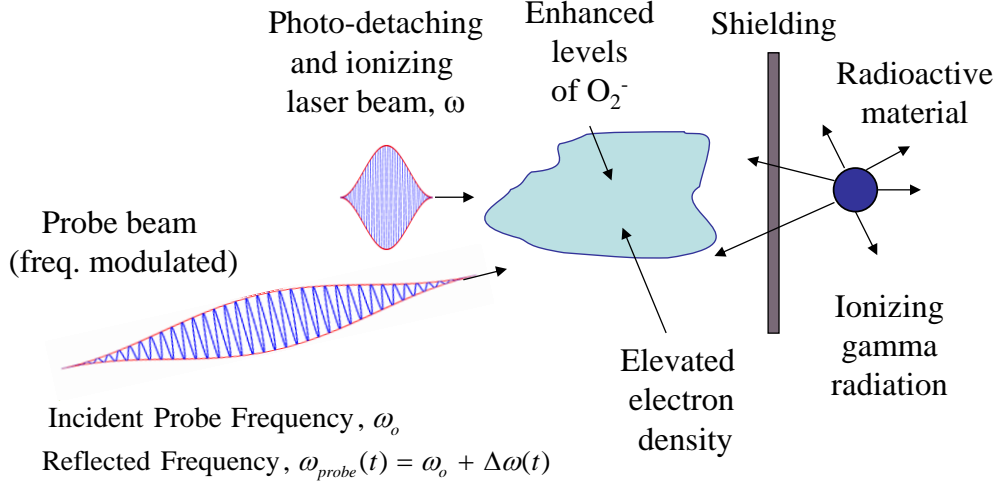
Figure 15. Schematic of active remote radioactivity detection concept. Laser radiation photo-detaches electrons from O_2^- ions, providing electrons for an avalanche (collisional) ionization process which increases the electron density. A probe beam in the presence of a temporally increasing electron density undergoes a frequency modulation which becomes a spectral signature of radioactivity.

To obtain the frequency modulation on a probe pulse it is necessary to follow the time evolution of the electron and negative ion density, which are sensitive functions of air chemistry processes and electron heating by the laser radiation. The source terms for the electrons include radioactivity, detachment, photo-detachment and photo-ionization, while the loss terms include various attachment and recombination processes including aerosols. The expressions for the rate of change of electron density N_e and negative ion density N_-, i.e., O_2^- in the present context, are [93],

$$\partial N_e / \partial t = (1 + \alpha_{rad}) Q_{rad} + S_e - L_e, \tag{12a}$$

$$\partial N_- / \partial t = S_- - L_-, \tag{12b}$$

where S_e represents the various electron source terms, L_e is the electron loss terms, S_- represents the ion sources, L_- is the ion loss terms and

$$\alpha_{rad} \approx \frac{\nu_{rad} \kappa_\gamma}{4\pi \langle L_{\gamma-e} \rangle} \frac{\langle E_e \rangle}{\Delta E} \frac{1}{Q_{rad}} \frac{\exp(-R/L_\gamma)}{R^2} \tag{13}$$

is the radiation enhancement factor. For a detailed discussion of the various terms in Eq.(12a,b) see Ref [93].

Since the free electron density is generally much less than the ion density, $N_e << N_-$ the steady state electron and negative ion densities are given by

$N_e \approx (\beta_n N_n / \eta)\sqrt{(1+\alpha_{rad})Q_{rad}/\beta_+}$, and $N_- \approx \sqrt{(1+\alpha_{rad})Q_{rad}/\beta_+}$, where

$\beta_+ \approx 2 \times 10^{-6}$ cm^3/sec is the recombination rate, $\eta \approx 10^8$ sec^{-1} is the attachment rate and $\beta_n \approx (5-10) \times 10^{-19}$ cm^3/sec is the negative ion detachment rate due to collisions with neutrals. In the absence of radioactive material ($\alpha_{rad}=0$) the ambient (background) electron and negative ion density are $N_e \approx 10^{-3}$ cm^{-3} and $N_- \approx 3 \times 10^3$ cm^{-3}, where $Q_{rad} = 20$ cm^{-3} sec^{-1}. At a distance of 4 m from a radioactive source containing 10 mg of ^{60}Co, the radioactive enhancement factor is $\alpha_{rad} \approx 2 \times 10^4$ and the elevated electron and negative ion densities are $N_e \approx 0.2$ cm^{-3} and $N_- \approx 4.7 \times 10^5$ cm^{-3}.

The various electron and ion source and loss terms in Eqs.(12a) and (12b), in particular the collisional ionization rate, are functions of the electron temperature. The electron temperature is determined by the collisional electron heating (Ohmic heating) by the laser radiation and the cooling effect resulting from excitation of vibrational modes of the air molecules. The equations for the electron temperature T_e is [93],

$$(3/2)\, \partial(N_e T_e)/\partial t = \langle \mathbf{J} \cdot \mathbf{E} \rangle - (3/2)(N_e / \tau_{cool})(T_e - T_{eo}), \qquad (14)$$

where T_e is the electron temperature, $\langle \mathbf{J} \cdot \mathbf{E} \rangle$ is the Ohmic heating rate, τ_{cool} is the electron cooling time due to inelastic collisions and $T_{eo} = 0.025$ eV is the ambient electron (room) temperature.

A probe beam with frequency ω_o propagating through a region of space in which the electron density is changing with time will undergo a frequency change. The electron density in the vicinity of the radioactive source and under the influence of the laser radiation varies in space and in time. The frequency of an electromagnetic probe beam propagating in such plasma will vary in space and in time. As an illustration we consider the case where the rise in electron density is exponential in time and spatially uniform within a region $0 \le z \le L$. Here the plasma frequency is given by

$\omega_p^2(z,t) = \omega_{po}^2 \exp(\nu_{ion} t)\, g(z)$, where ν_{ion} is the effective ionization rate and

$g(z)=1$, $0 \le z \le L$, defines the axial extent of the plasma region. The frequency modulation on the probe beam is given by $\omega_{probe}(z,t) = \omega_o + \Delta\omega(z,t)$, where

$$\Delta\omega(z,t) = \omega_{po}^2/(2\omega_o)\exp(\nu_{ion}t)(1 - \exp(-\nu_{ion}z/c)). \qquad (15)$$

The maximum fractional frequency shift occurs for $z > c/\nu_{ion} \sim 1\,\text{cm}$ and is $\Delta\omega_{max}/\omega_o = (\omega_{po}^2/2\omega_o^2)\exp(\nu_{ion}t)$. The effective ionization rate can vary widely but is typically $\nu_{ion} \sim 10^{11}\,\text{sec}^{-1}$. The frequency modulation on the probe beam can be substantial and is readily measurable.

To illustrate the radioactivity detection concept we consider the following example. In the numerical examples the system quantities, i.e., electron density, ion density, electron temperature and frequency modulation on a probe laser, are calculated both in the absence ($\alpha_{rad} = 0$) and in the presence of radioactive material by numerically solving the full set of coupled equations. The radioactive source is assumed strong enough to produce a radiation enhancement factor of $\alpha_{rad} = 10^3$. We take the ionizing laser to have a peak intensity of $I_{peak} = 160\,\text{GW/cm}^2$ and pulse duration of $\tau_{laser} = 1\,\text{nsec}$. In these examples, the probe beam is taken to be a millimeter wave source of frequency $f_{probe} = 94\,\text{GHz}$, ($\lambda_{probe} = 3.2\,\text{mm}$). The background radiation is taken to be $Q_{rad} = 30$ disintegrations/(cm^3 − sec).
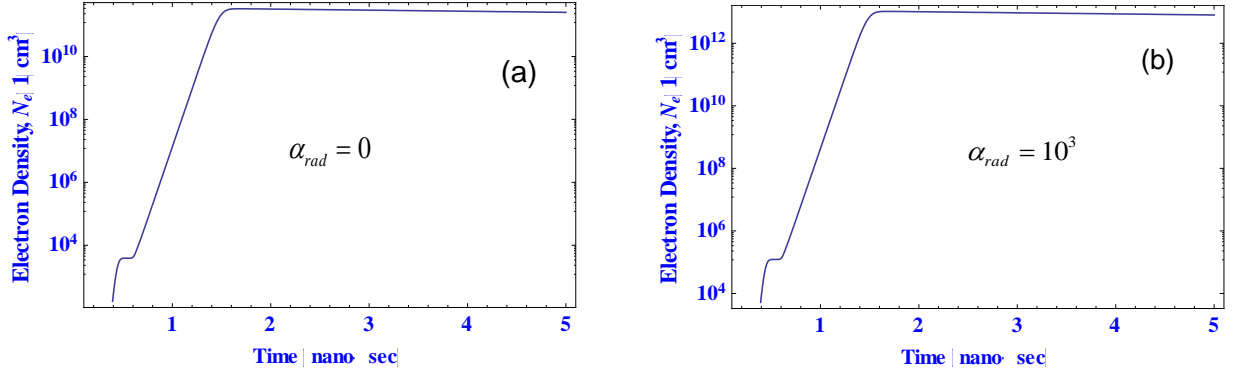
Figure 16. Electron density as a function of time, (a) background radiation only ($\alpha_{rad} = 0$), (b) in the presence of radioactivity ($\alpha_{rad} = 10^3$). The laser parameters are, $\lambda = 1\mu m$, $I_{peak} = 160$ GW/cm^2 and $\tau_{laser} = 1$nsec.

In the absence of a radioactive source, Fig.16(a), the ionizing laser intensity is just below the breakdown level, i.e., the electron density is low, and there is virtually no frequency modulation on the probe beam. Figure 16(b) shows the electron density as a function of time in the presence of radioactive material ($\alpha_{rad} = 10^3$). The electron density at the end of the ionizing laser pulse approaches the value of $N_e = 10^{13}$ cm^{-3} which is an order of magnitude less than the critical electron density.

The frequency modulation on the probe millimeter wave beam is shown in Fig.17. In the absence of radioactive material there is no frequency modulation on the probe. However, for $\alpha_{rad} = 10^3$ the fractional frequency modulation is significant and equal to $\sim 5\%$, which is readily detectable.
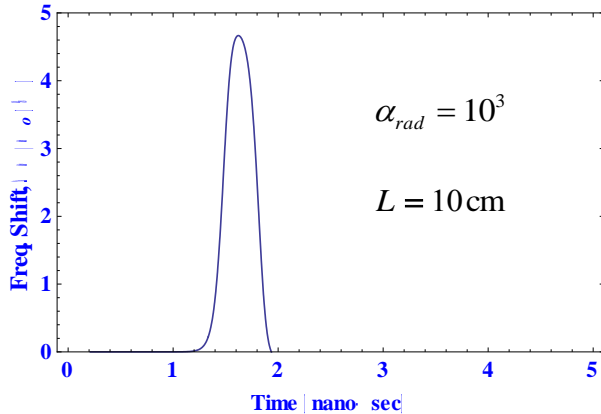

Figure 17. Fractional frequency shift $\Delta\omega / \omega_o$ [%] versus time in the presence of radioactive material $\alpha_{rad} = 10^3$ at the probe interaction distance of $L = 10$cm. The laser parameters are the same as in Fig.16.

b) Atmospheric Lasing

Nitrogen lasers are typically based on collisional excitation using electrical discharges [94-96]. In this section we discuss a remote atmospheric lasing mechanism [97] in which an ultrashort pulse laser forms a plasma filament (seed electrons) by tunneling ionization and a heater pulse thermalizes the seed electrons. The thermal electrons collisionally excite nitrogen molecules and induce lasing in the ultraviolet. A remote atmospheric lasing configuration based on collisionally exciting the N_2 lasing line at $\lambda = 337\,\mathrm{nm}$ in a heated plasma filament, as illustrated in Fig.18. The lasing gain is sufficiently high to reach saturation within the length of the plasma filament. A remotely generated ultraviolet source may have applications for standoff detection of biological and chemical agents.
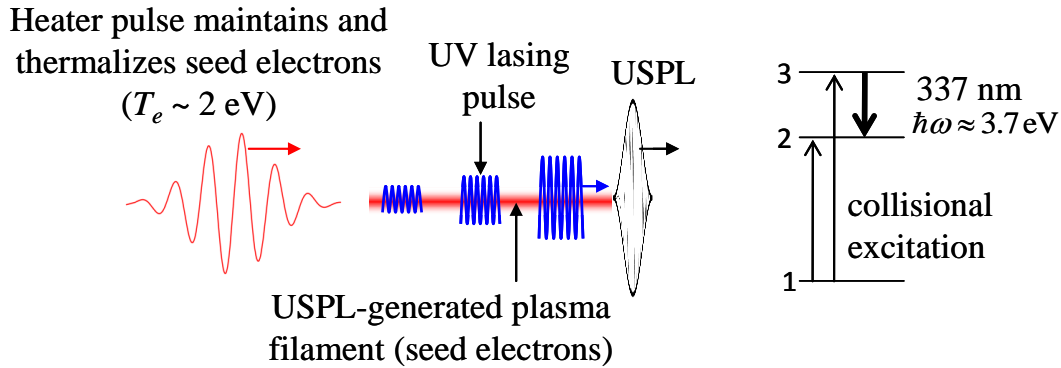

Figure 18. Schematic diagram of remote lasing configuration. An ultrashort pulse laser creates a plasma filament of seed electrons that is heated by a secondary heater pulse. In the energy level diagram for N_2 (right), the energetic electrons collisionally excite the N_2 molecules and induce lasing.

A heater laser pulse is used to maintain and thermalize the electrons. Thermal electrons of a few eV can induce a population inversion in N_2 leading to the vibrational-electronic transition $C^3\Pi_u \rightarrow B^3\Pi_g$ at 337 nm. In the present configuration the UV radiation is generated in both the forward and backward directions along a filament with a gain sufficiently high to reach saturation. For a $1\mu\mathrm{m}$ wavelength heater beam the Kerr

nonlinearity can be the source of third harmonic generation and a seed for lasing at 337 nm.

To analyze the lasing process the density matrix and Maxwell equations [97] together with the electron heating and ionization equations are solved. The N_2 lasing model consists of an open two level system denoted by levels 3 (upper) and 2 (lower) respectively. Since levels 3 and 2 are weakly excited the population of level 1 (ground) is taken to be fixed. The population of the excited levels are given by

$$\partial N_3 / \partial \tau = \nu_{CE,13} N + \nu_{CE,23} N_2 - \nu_3 N_3 - \nu_{stim} \Delta N, \qquad (16a)$$

$$\partial N_2 / \partial \tau = \nu_{CE,12} N + (\nu_{CD,32} + \Gamma_{32}) N_3 - \nu_2 N_2 + \nu_{stim} \Delta N, \qquad (16b)$$

where $\tau = t - z/c$, z is the position within the filament, N_n, are densities of the nth level, $N \approx N_1 = 0.8 N_{air}$ is the ground state nitrogen density, $N_{air} = 2.7 \times 10^{19} \, \text{cm}^{-3}$ is the air density, $\nu_3 = \nu_{CD,31} + \nu_{CD,32} + \Gamma_{31} + \Gamma_{32}$ is the decay rate of level 3, $\nu_2 = \nu_{CD,21} + \nu_{CE,23} + \Gamma_{21}$ is the decay rate of level 2, Γ_{ij} is the radiative (spontaneous) decay from level i to j, $\nu_{CE,ij}$ is the collisional excitation rate from level i to j, and $\nu_{CD,ij}$ is the collisional de-excitation rate from level i to j ($i, j = 1, 2, 3$), $\nu_{stim} = \sigma_{stim} I / \hbar \omega$ is the stimulated emission rate, I is the UV laser intensity, ω is the lasing frequency σ_{stim} is the stimulated emission cross section and $\Delta N = N_3 - N_2$. The collisional excitation rates are dominated by electron excitations while the de-excitation rates are dominated by molecular collisions.

The lasing intensity is given by

$$(\partial / \partial z + \Gamma_d) I = \varepsilon I_{stim} / (c \tau_{rad}) + \sigma_{stim} \Delta N I, \qquad (17)$$

where Γ_d is the spatial damping rate, ε is a geometric filling factor associated with the seed radiation within the plasma filament, $I_{stim} = \hbar \omega c N_3$ and τ_{rad} is the radiative lifetime from level 3 to 2 including the effects of collisions.

Figure 19 plots the temporal profile of the UV radiation and population inversion at various positions along the filament. Here, the heating pulse duration is $\tau_o = 0.4 \, \text{nsec}$, and the intensity is $I_o = 7 \times 10^{11} \, \text{W/cm}^2$. Figure 19 shows a UV pulse (~ 0.1 nsec long) forming near the back of the inversion region. As the UV pulse grows ΔN is depleted

and the peak of the UV pulse moves forward relative to the heater pulse. After ~ 2 cm of propagation, the peak UV intensity is ~ 8 MW/cm^2 and the fluence is ~ 0.5 mJ/cm^2. The peak electron temperature is typically ~ 2.5 eV within the heater pulse.

Lasing will occur in both the forward and backward directions when the length of the heated plasma filament is longer than the saturation distance. For the numerical examples given here this condition is satisfied. The length of the heated plasma filament is ~ 6 cm, while the lasing saturation lengths are typically ~ 1-3 cm. It should be mentioned that other molecular transitions may also be excited and result in lasing, e.g., N_2^+ and O_2.
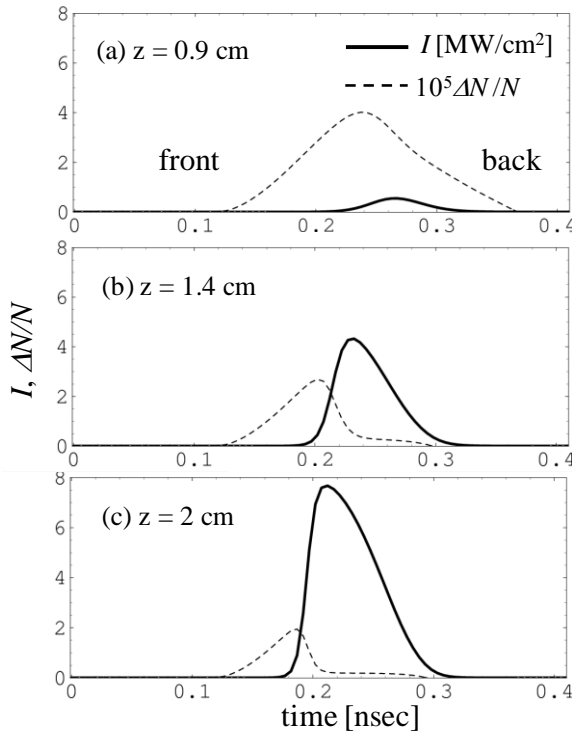

Figure 19. UV intensity, I (solid curves) and normalized population inversion $\Delta N / N = (N_3 - N_2) / N$ (dashed curves) as functions of time at (a) $z = 0.9\,\text{cm}$, (b) $z = 1.4\,\text{cm}$, and (c) $z = 2\,\text{cm}$, for a heating pulse with $\lambda_o = 1\,\mu m$, $I_o \tau_o = 285\,\text{J/cm}^2$ and pulse duration $\tau_o = 0.4\,\text{nsec}$

VI. Concluding Remarks: A number of topics associated with high-power, high-intensity lasers have been discussed. The aim has been to briefly illustrate the varied physical processes and phenomena that are manifested in the interaction of these lasers with matter. We have also described some of the actual and potential applications of high-power as well as high-intensity lasers. This paper is not intended to be an exhaustive overview of the various topics; important references on the topics may have been omitted.

References

1. T.C. Marshall, *Free-electron lasers* (Macmillan, NY, USA, 1985).

2. C.W. Roberson and P. Sprangle, Phys. Fluids **1**, 3 (1989).

3. H.P. Freund and T.M. Antonsen, *Principles of free-electron lasers* (Chapman & Hall, London, UK, 1992).

4. J.M.J. Madey, J. Appl. Phys. **42**, 1906 (1971).

5. P. Sprangle, J. Plasma Phys. **11**, 299 (1974).

6. P. Sprangle and V.L. Granatstein, Appl. Phys. Lett. **25**, 377 (1974).

7. L.R. Elias, W.M. Fairbank, J.M.J. Madey, H.A. Schwettman and T.I. Smith, Phys. Rev. Lett. **36**, 717 (1976).

8. W.B. Colson, Phys. Lett. **A 64**, 190 (1977).

9. A.A. Kolomenskii and A.N. Lebedev, Sov. J. Quantum Electron. **8**, 879 (1978).

10. P. Sprangle and A. T. Drobot, J. Appl. Phys. **50**, 2652 (1979).

11. P. Sprangle, C. M. Tang and W.M. Manheimer, Phys. Rev. A **21**, 302 (1980).

12. N.M. Kroll, P.L. Morton and M.N. Rosenbluth, IEEE J. Quantum Electron. **QE-17**, 1436 (1981).

13. P. Sprangle and C. M. Tang, Appl. Phys. Lett. **39,** 9 (1981).

14. S. Reiche, Nucl. Instrum. Methods Phys. Research A **429**, 243 (1999).

15. A. Ting and P. Sprangle, Particle Accel. **22**, 149 (1987).

16. P. Sprangle, J. Penano, B. Hafizi, D. Gordon, S. Gold, A. Ting and C. Mitchell, Phys. Rev. Special Topics Accelerators and Beams **14**, 020702 (2011).

17. Linac Coherent Light Source Conceptual Design Report, SLAC-R-593, UC-414, SLAC (2002).

18. TESLA Technical Design Report, TESLA FEL 2002-09, DESY, (2002).

19. SPring-8 Compact SASE Source Conceptual Design Report, http://www-xfel.spring or.jp (2005).

20. I. S. Ko, in *Proceedings of the 2005 Free Electron Laser Conference* (Stanford, CA, USA, 2005).

21. K.J. Kim, Phys. Rev. Lett. **57**, 1871 (1986).

22. C. Pellegrini, Nucl. Instrum. Methods Phys. Research **A 445**, 124 (2000).

23. Z. Huang and K.J. Kim, Nucl. Instrum. Meth. Phys. Research A **507**, 65 (2003).

24. P. Sprangle, B. Hafizi and J. Penano, Phys. Rev. Special Topics, Accel. and Beams **12**, 050702 (2009).

25. P. Sprangle, B. Hafizi and F. Mako, Appl. Phys. Lett. **55**, 2559 (1989).

26. P. Sprangle, A. Ting. E. Esarey and A. Fisher, J. Appl. Physics **72**, 5032 (1992).

27. E. Esarey, S.K. Ride and P. Sprangle, Phys. Rev. E **48**, 3003 (1993).

28. V. Malkin, G. Shvets and N. Fisch, Phys. Rev. Lett. **82**, 4448 (1999).

29. N. Fisch and V. Malkin, Phys of Plasmas **10**, 2056 (2003).

30. R.M.G.M. Trines, F. Fiuza, R. Bingham, R. Fonseca, L. Silva, R. Cairns and P. Norreys, Nature Physics **7,** 87 (2011).

31. W. Cheng, Y. Avitzour, Y. Ping, S. Suckewer, N. Fisch, M. Hur and J. Wurtele, Phys. Rev. Lett. 94, 045003 (2005).

32. J. Ren, W. Cheng, S. Li and S. Suckewer, Nature Physics **3**, 732 (2007).

33. G. A. Mourou, T. Tajima and S. V. Bulanov. Reviews of Modern Physics, **78** 309 (2006).

34. A. Braun, G. Korn, X. Liu, D. Du, J. Squier, and G. Mourou, Opt. Lett. **20**, 73 (1995).

35. E.T. Nibbering, P.F. Curley, G. Grillon, B. S. Prade, M.A. Franco, F. Salin, and A. Mysyrowicz, Opt. Lett. **21**, 1 (1996).

36. O.G. Kosareva, V.P. Kandidov, A. Brodeur, C.Y. Chien, and S.L. Chin, Opt. Lett. **22**, 1332 (1997).

37. L. Woste, C. Wedekind, H. Wille, P. Rairoux, B. Stein, S. Nikolov, Ch. Werner, St. Niedermeier, F. Ronneberger, H. Schillinger, and R. Sauerbrey, Laser Optoelektron **29**, 51 (1997).

38. B. La Fontaine, F. Vidal, Z. Jiang, C.Y. Chien, D. Comtois, A Desparois, T.W. Johnston, J.-C. Kieffer, H. Pepin, and H.P. Mercure, Phys. Plasmas **6**, 1615 (1999).

39. J. Kasparian, R. Sauerbrey, D. Mondelain, S. Niedermeier, J. Yu, J.-P. Wolf, Y.-B. Andre, M. Franco, B. Prade, S. Tzortzakis, A. Mysyrowicz, M. Rodriguez, H. Wille, and L. Woste, Opt. Lett. **25**, 1397 (2000).

40. P. Sprangle, J. R. Peñano, and B. Hafizi, Phys. Rev. E **66**, 046418 (2002).

41. A. Couairon and A. Mysyrowicz, Phys. Reports **441**, 47 (2007).

42. A. Ting, D. Gordon, D. Kaganovich, E. Briscoe, C. Manka, P. Sprangle, J. Peñano, B. Hafizi, and R. Hubbard, J. Directed Energy 1, 131 (2004).

43. A. Ting, I. Alexeev, D. Gordon, E. Briscoe, J. Penano, R. Fischer, R. Hubbard, P. Sprangle and G. Rubel, Applied Optics **44**, 5315 (2005).

44. S. Varma, Y.-H. Chen and H. M. Milchberg, Phys. Rev. Lett. **101**, 205001 (2008).

45. S. Eisenmann, J. Peñano, P. Sprangle and A. Zigler, Phys. Rev. Lett. **100**, 155003 (2008).

46. X. Xie, J. Dai and X. Zhang, Phys. Rev. Lett. **96**, 075005 (2006).

47. K.Y. Kim, Phys of Plasmas **16**, 056706 (2009).

48. R.W. Boyd, *Nonlinear Optics* (Academic Press, San Diego, 1992).

49. P. Milonni and J.H. Eberly, *Lasers* (Wiley, New York, 1988).

50. M. Capitelli, C.M. Ferreira, B.F. Gordiets and A.I. Osipov, *Plasma Kinetics in Atmospheric Gases* (Springer-Verlag, NY, 2010).

51. Ya.B. Zel'dovich and Yu. P. Raizer, *Physics of Shock Waves and High-Temperature Hydrodynamic Phenomena* (Dover, Mineola, NY, 2002).

52. R. Schunk and A. Nagy, *Ionospheres* (Cambridge University Press, Cambridge, UK, 2009).

53. R.F. Fernsler and H.L. Rowland, J. Geophys. Res. **101**, 29653 (1996).

54. P. Sprangle, E. Esarey, A. Ting and G. Joyce, Appl. Phys. Lett. **53**, 2146 (1988).

55. T.M. Antonsen and P. Mora, Phys. Fluids B**5**, 1440 (1993).

56. P. Sprangle, J. Krall and E. Esarey, Phys. Rev. Lett. **73**, 3544 (1994).

57. J. Krall, A. Ting, E. Esarey and P. Sprangle, Phys. Rev. E **48**, 2157 (1993).

58. D. Umstadter, S.Y. Chen, A. Maksimchuk, G. Mourou and R. Wagner, Science **273**, 472 (1996).

59. E. Esarey, P. Sprangle, J. Krall and A. Ting, IEEE Trans. Plasma Sci. **24**, 252 (1996).

60. A. Modena, Z. Najmudin, A.E. Dangor, C.E. Clayton, K.A. Marsh, C. Joshi, V. Malka, C.B. Darrow and C. Danson, IEEE Trans. Plasma Sci. **24**, 289 (1996).

61. C.I. Moore, A. Ting, K. Krushelnick, E. Esarey, R.F. Hubbard, B. Hafizi, H.R. Burris, C. Manka and P. Sprangle, Phys. Rev. Lett. **79**, 3909 (1997).

62. P. Mora and T.M. Antonsen, Phys. Plasmas **4**, 217 (1997).

63. W.B. Mori, IEEE J. Quantum Electronics, **33**, 1942 (1997).

64. E. Esarey, P. Sprangle, J. Krall and A. Ting, IEEE Trans. Plasma Sci. **33**, 1879 (1997).

65. D. Gordon, K.C. Tzeng, C.E. Clayton, A.E. Dangor, V. Malka, K.A. Marsh, A. Modena, W.B. Mori, P. Muggli, Z. Najmudin, D. Neely, C. Danson and C. Joshi, Phys. Rev. Lett. **80**, 2133 (1998).

66. P. Sprangle and B. Hafizi, Phys. Plasmas **6**, 1683 (1999).

67. F. Dorchies, J. R. Marques, B. Cros, G. Matthieussent, C. Courtois, T. Velikoroussov, P. Audebert, J. P. Geindre, S. Rebibo, G. Hamoniaux and F. Amiranoff, Phys. Rev. Lett. **82**, 4655 (1999).

68. P. Sprangle, B. Hafizi and J. Penano, Phys. Rev. E **61**, 4381 (2000).

69. B. Hafizi, A. Ting, P. Sprangle and R.F. Hubbard, Phys. Rev. E **62**, 4120 (2000).

70. K. Krushelnick, A.Ting, C.I. Moore, H. R. Burris, E. Esarey, P. Sprangle and M. Baine, Phys. Rev. Lett. **78**, 4047 (1997).

71. Y. Ehrlich, C. Cohen, D. Kaganovich, A. Zigler, R.F. Hubbard, P. Sprangle and E. Esarey, J. Opt. Soc. Am. B **15**, 2416 (1998).

72. D. Kaganovich, A. Ting, C.I. Moore, A. Zigler, H. R. Burris, Y. Ehrlich, R. Hubbard and P. Sprangle, Phys. Rev. E **59**, R4769 (1999).

73. A.B. Borisov, A.V. Borovskiy, O.B. Shiryaev, V.V. Korobkin A. M. Porokhorov, J.C. Solem, T.S. Luk, K. Boyer and C.K. Rhodes, Phys. Rev. A **45**, 5830 (1992).

74. C.G. Durfee III and H. M. Milchberg, Phys. Rev. Lett. **71**, 2409 (1993).

75. C.G. Durfee III, T.R. Clark, and H.M. Milchberg, J. Opt. Soc. Am. B **13**, 59 (1996).

76. H.M. Milchberg, T.R. Clark, C.G. Durfee, T.M. Antonsen and P.Mora, Phys. Plasmas **3**, 2149 (1996).

77. R.F. Hubbard, D.F. Gordon, J.H. Cooley, B. Hafizi, T.G. Jones, D. Kaganovich, P. Sprangle, A.C. Ting, A. Zigler and J. Dexter, IEEE Trans. Plasma Sci. **33**, 712 (2005).

78. W.P. Leemans, B. Nagler, A.Goansalves, C. Toth, K. Nakamura, C. Geddes, E. Esarey, C. Schroder and S. Hooker, Nature Physics **2**, 696 (2006).

79. P. Sprangle, E. Esarey, and A. Ting, Phys. Rev. A **41**, 4463 (1990).

80. P. Sprangle, B. Hafizi, J.R. Penano, R.F. Hubbard, A. Ting, A. Zigler, and T.M. Antonsen, Jr., Phys. Rev. Lett. **85**, 5110 (2000).

81. P. Sprangle, B. Hafizi, J. Penano, R.F. Hubbard, A. Ting, C.I. Moore, D. Gordon, A. Zigler, D. Kaganovich and T.M. Antonsen, Jr., Phys. Rev. E. **63**, 056405 (2001).

82. B.D. Layer, A.G.York, S. Varma, Y.-H. Chen and H. Milchberg, Optics Express, 17 4263 (2009)

83. R.L. Fante, Proc. IEEE **63**, 1669 (1975).

84. P. Sprangle, J. Penano, and B. Hafizi, J. Directed Energy **2**, 71 (2006).

85. P. Sprangle, A. Ting, J. Penano, R. Fischer and B. Hafizi, IEEE J. Quantum Electron. **45**, 138 (2009).

86. J. Penano, P. Sprangle and B. Hafizi, J. Directed Energy **2**, 107 (2006).

87. A. Khizhnyak, V. Markov and F.Wu, Proc. SPIE 6878, 68780D (2008).

88. P. Sprangle, J. Penano, V. Markov, A. Khizhnyak, A. Ting, B. Hafizi, C.C. Davis and L. DeSandre, Proc. SPIE 8535, Optics in Atmospheric Propagation and Adaptive Systems XV, 85350F (Nov. 8, 2012).

89. A.E. Siegman, P.A. Belanger and A. Hardy, in *Optical Phase Conjugation*, R. A. Fisher (ed.), Academic press, New York, 1983.

90. M.D. Skeldon, P. Narum and R. W. Boyd, Opt. Lett. 12, 343 (1987).

91. V.L. Granatstein and G.S. Nusinovich, J. Appl. Phys. **108**, 063304 (2010).

92. G.S. Nusinovich, R.Pu, T.M. Antonsen, O.V. Sinitsyn, J.Rodgers, A.Mohamed, J. Silverman, M.Al-Sheikhly, Y.S. Dimant, G.M. Milikh, M.Yu, Glyavin, A.G. Luchinin, E.A. Kopelovich and V.L. Granatstein, J. Infrared Milli. Terahz. Waves, **32** 380 (2011).

93. P. Sprangle, B. Hafizi, H. Milcherg, G. Nusinovich and A. Zigler, Phys. of Plasmas, **21**, 013103 (2014).

94. E.T. Gerry, Appl. Phys. Lett. **7**, 6 (1965).

95. A.W. Ali, A.C. Kolb and A.D. Anderson, Appl. Opt. **6**, 2115 (1967).

96. R.T. Brown, J. Appl. Phys. **46**, 4767 (1975).

97. P. Sprangle, J. Penano, B. Hafizi, D. Gordon and M. Scully. Appl. Phys. Lett. **98**, 211102 (2011).